Mass-Spring Model for Simulation of Heart Valve Tissue Mechanical Behavior

Peter E. Hammer[1,2,4,*], Michael S. Sacks[3], Pedro J. del Nido[1] , Robert D. Howe[4]

[1]Department of Cardiac Surgery, Children's Hospital, Boston, MA

[2]Department of Biomedical Engineering, Tufts University, Medford, MA

[3]Department of Bioengineering, University of Pittsburgh, Pittsburgh, PA

[4]Harvard School of Engineering and Applied Sciences, Cambridge, MA

Abbreviated title: Mass-Spring Model for Simulation of Heart Valve Tissue

* Address correspondence to: Peter E. Hammer, Department of Cardiac Surgery,

Children's Hospital, 300 Longwood Ave., Boston, MA, USA. E-mail address:

peter.hammer@childrens.harvard.edu.

Abstract

Heart valves are functionally complex, making surgical repair difficult. Simulation-based surgical planning could facilitate repair, but current finite element (FE) studies are prohibitively slow for rapid, clinically-oriented simulations. Mass-spring (M-S) models are fast but can be inaccurate. We quantify speed and accuracy differences between an anisotropic, nonlinear M-S and an efficient FE membrane model for simulating both biaxial and pressure loading of aortic valve (AV) leaflets. The FE model incurs approximately ten times the computational cost of the M-S model. For simulated biaxial loading, mean error in normal strains is <1% for both FE and M-S models for equibiaxial loading but increases for non-equibiaxial states for the M-S model (7%). The M-S model was less able to simulate shear behavior, with mean strain error of approximately 80%. For pressurized AV leaflets, the M-S model predicts similar leaflet dimensions to the FE model (within 2.6%), and the coaptation zone is similar between models. The M-S model simulates in-plane behavior of AV leaflets considerably faster than the FE model and with only minor differences in the deformed mesh. While the M-S model does not allow explicit control of shear response, shear does not strongly influence shape of the simulated AV under pressure.

Introduction

Heart valves are thin, membrane-like structures that control the direction of blood flow through the heart. Valve dysfunction can lead to heart failure and death, and surgery is the primary treatment option. Surgical repair of heart valves is difficult due to their intricate structure and complex properties; biomechanical studies have shown that leaflets of heart valves exhibit an anisotropic, nonlinear stress-strain relationship and large deformations under physiological loads [3, 19, 23, 29]. Furthermore, repairs are normally performed during open heart surgery when the heart is emptied of blood and the valves are motionless, making it difficult for the surgeon to know how a given surgical modification will translate into valve function after the heart has been closed and blood flow restored. A surgical simulator based on patient-specific medical images has been proposed as a way to improve surgical outcomes [16]. Under the proposed scheme, pre-operative images are acquired, and a computational mesh of the malfunctioning valve is generated. The surgeon explores potential repair strategies on the computer model of the open valve then uses simulation to predict the closed state of the valve. For this surgical planning environment to be of practical use to a surgeon, simulations must be fast - no more than a few minutes per valve closing cycle – so that multiple surgical repair strategies could be simulated in succession, with feedback from one simulated repair guiding the subsequent simulated repair in an iterative process.

Published computational models of heart valves use the finite element (FE) method to study normal, pathological and prosthetic valves and to evaluate innovative devices or methods for surgical repair [7, 14, 18-21, 26, 27, 34, 36]. The FE method can provide accurate approximation to the behavior of continua. However, FE simulations of heart valves are typically slow due to large

deformations, complex constitutive laws, and numerical stiffness of the system equations. While most heart valve FE studies do not report simulation times, a recent FE model of the mitral valve developed for surgical planning reports simulating one closing cycle in 81 hours, and simulation time drops to 7.5 hours using a high performance computing cluster with 32 parallel CPU's [35]. Speed limitations have precluded use of computational models for patient-specific surgical planning and for real-time surgical simulation of heart valves.

Mass-spring (M-S) models have been used to simulate deformable surfaces [5, 8, 32], and they can typically be computed at rates much faster than continuum methods due to their computational simplicity. M-S models can be applied to either structured or unstructured meshes, although only unstructured meshes will be considered here due to their predominance in automatic mesh generation methods. M-S models are fundamentally discrete, and they can be a poor approximation to the underlying continuum [13]. This is especially true of unstructured meshes. Van Gelder has proposed a simple method for choosing spring stiffness to minimize inhomogeneities in deformation due to the mesh [32]. Other groups have proposed optimization methods for tuning individual spring stiffness throughout a given mesh to approximate specific behavior of the overall surface [2, 9, 22]. These methods, however, involve considerable precomputation, which can be problematic for a surgical planning system where the mesh is modified prior to each simulation. In their simplest form, M-S models define an elastic force between two vertices that varies with edge length. However, variants have been proposed to simulate various material properties. For example, Bourguignon et al proposed a M-S method for handling anisotropy by restricting all internal forces to axes aligned with local principal material axes instead of mesh edges [4]. Delingette presented a method for simulating isotropic hyperelastic

4

membranes using a new type of spring, which is based on finite strain mechanics and allows a formal connection between FE and M-S methods [8].

For fast simulation of heart valve closure for use in patient-specific surgical planning, the decision of whether to use M-S or continuum-based methods for modeling the valve leaflets hinges on the relative accuracy and computational cost of these methods. In this study, we assess this trade-off between speed and accuracy. We present a M-S model that approximates the anisotropic, nonlinear in-plane behavior of aortic valve leaflet tissue on unstructured triangular meshes, and compare the accuracy and computational cost of M-S and FE models. Both models are implemented in the same programming environment so that they can be run on the same input meshes and using the same solvers, allowing us to directly compare computational speed and accuracy. To assess accuracy of the models, we first compared stress-strain curves of simulated square patches of membrane under biaxial loading to stress-strain curves calculated directly from the constitutive law. We then simulate pressure loading of aortic valve leaflets at end-diastole - both a single leaflet of an aortic valve and a full valve consisting of three leaflets - and we compare critical dimensions of the deformed meshes produced by both the M-S and FE methods. Simulations of biaxial loading illustrate the aspects of material behavior that the M-S model can and cannot accurately capture, while pressure loading simulations help assess model behavior as it is relevant for heart valves.

Methods

Continuum model for aortic valve leaflet tissue.

To simulate the in-plane response, the following Fung-type constitutive law was used to approximate the leaflet response

5

$$S_{ij} = \frac{\partial W}{\partial E_{ij}} \qquad (1)$$

where S is the second Piola-Kirchhoff stress tensor, E is the Green strain tensor, i and j are indices representing the two principal directions, and W is strain energy density. We assume an exponential form for W after Fung [11]

$$W = \frac{c}{2}\left(e^Q - 1\right) \qquad (2)$$

where c is a constant and Q represents the following combination of components of the Green strain tensor:

$$Q = A_1 E_{11}^2 + A_2 E_{22}^2 + 2A_3 E_{11} E_{22} + A_4 E_{12}^2 + 2A_5 E_{11} E_{12} + 2A_6 E_{22} E_{12} \qquad (3)$$

The values A are constants, and these along with c are determined with a Levenberg-Marquardt nonlinear curve fitting algorithm[28] carried out in the coordinate system aligned with the principal axes using data from previously published biaxial experiments on normal aortic valve leaflet tissue[29].

Computational models of anisotropic membrane

Mesh Generation. For simulations of biaxial loading, a square patch 15 mm on a side was meshed into a given number of triangles by randomly scattering points within the square then repeatedly connecting the points using Delaunay triangulation and adjusting the positions of all points interior to the boundaries by treating all triangle edges as springs with equal spring constant and resting length and solving for the global equilibrium position of the interior points. This process of triangulating and adjusting the nodes typically converged after 8-10 iterations to a set of nearly equilateral triangles. In order to characterize the variability in simulation results due to mesh discretization, biaxial test simulations were performed on a set of 10 meshes with

similar number of triangles (229 +/- 1) and similar mean triangle quality (0.95). We assess triangle quality as $q = 4a\sqrt{3}/(s_1^2 + s_2^2 + s_3^2)$, where a is the area of the triangle and s_i are the lengths of its three sides[10]. This index equals 1.0 for an equilateral triangle, and $q = 0.6$ is generally considered as a threshold below which numerical approximation and/or stability may suffer, although in practice this threshold is highly problem-dependent.

For simulations of aortic valves, a single leaflet was represented as a semicircle with diameter of 20 mm fixed along its semi-circumference to the inside wall of a cylinder with circumference of 60 mm. Again, a set of 10 semicircular meshes with similar number of triangles (221+/- 2) and similar mesh quality (0.95) was generated and used for simulations of a pressure loaded leaflet. A complete aortic valve model was produced by combining three identical semicircular leaflets arranged circumferentially around the inside wall of the cylinder (Fig. 1). Mesh generation used the same method as for the square patch.

Equations of Motion. Response of the patch to both biaxial and pressure loading was simulated by computing the net force on all mesh nodes due to internal forces (*i.e.,* deformation) then equating these forces with damping forces, inertial forces, and externally applied loads and solving the resulting system of ordinary differential equations to update nodal positions. The finite element model and mass-spring models compared in this study differ only in how they compute the internal forces. The following sections describe the M-S and FE methods for computing these internal forces.

Internal Forces for Mass-Spring Model. We model an unstructured triangular mesh as a M-S system by treating each triangle edge as a spring (Fig. 2A). The mass of each triangular element, computed as the product of its area, thickness and density, is distributed equally among its three vertices. The force in each triangle edge (spring) is computed as the product of the magnitude of the deflection of the spring from its resting length, the spring constant, and the unit vector describing the present direction of the edge. We wish to choose spring constants to approximate the nonlinear anisotropic in-plane behavior described by Eqns. (1-3). Since our goal is simulating heart valves under uniform pressure loading, we make the simplifying assumption that the two stress-strain curves corresponding to equibiaxial loading (one curve for the fiber direction and one for the cross-fiber direction) sufficiently describe the in-plane response. We approximate each of these curves with a piecewise linear fit consisting of a segment of slope m_1 passing through the origin and a second segment of slope m_2 intersecting the first segment at some critical value of Green strain, which we express as stretch ratio λ^* (Fig. 2B). For a given spring at angle ϕ with respect to the material fiber direction, in-plane behavior at some intermediate angle between the fiber and cross-fiber directions is computed by assuming that these piecewise fits vary smoothly with direction ϕ. Specifically, slope m_1 for example, varies with ϕ according to $m_1(\phi) = \sqrt{m_{1f}^2 cos^2\phi + m_{1c}^2 sin^2\phi}$, where m_{1f} is the initial slope in the fiber direction and m_{1c} is the initial slope in the cross-fiber direction. The other parameters, m_2 and λ^*, vary similarly and can be computed for every spring in the mesh based on the angle ϕ in the undeformed state of the mesh.

To compute the spring constant for a given spring, we use an equation proposed by van Gelder for calculating spring constants throughout an unstructured triangular mesh in order to produce uniform membrane behavior [32]

$$k_c = \frac{Eh \sum_i area(T_i)}{|c|^2} \tag{4}$$

where k_c is the spring constant for edge c of a given triangle, E is Young's modulus for the leaflet tissue, h is leaflet thickness which is assumed uniform and equal to 0.5 mm, the summation term represents the area of all triangles sharing edge c, and the denominator is the squared length of edge c. In place of Young's modulus, E, we use the slope m_1 or m_2, depending on whether the present deformation of the spring corresponds to a value of stretch less than or greater than λ^*.

Two spring constants for each spring, one for small and one for large displacements, are pre-computed at the start of a simulation as is the stretch ratio, λ^*, at which each spring undergoes its change in stiffness. During the simulation, the force in a given spring is computed as

$$\vec{f} = k_1(l - l_0)\hat{n} \tag{6}$$

for springs with stretch magnitude less than λ^* and as

$$\vec{f} = \left(k_1 l_0(\lambda^* - 1) + k_2(l - \lambda^* l_0)\right)\hat{n} \tag{7}$$

for springs with stretch magnitude greater than λ^*. In these equations, k_1 and k_2 are spring constants for the low and high stiffness regimes of the spring, respectively, l is the present length of the spring, l_0 is the rest length of the spring and n is the unit vector describing the present direction of the spring. The force in the spring is then applied to the two nodes bounding it, and the net internal force on each node in the mesh is computed by summing the contributions of all springs sharing a given node.

Internal Forces for Finite Element Model. In order to evaluate the computational cost of a finite element model of an anisotropic membrane as well as to have a reference to which to compare accuracy of the M-S model simulations, a FE model formulated for large deformations and unstructured triangular meshes was implemented. We use a model presented by Taylor et al. that was derived directly from membrane assumptions rather than by simplifying shell theory [30]. This results in a conceptually and computationally straightforward formulation. The basic equations are reproduced here, but the reader is referred to the cited source for a more thorough presentation.

The Green strain tensor for a given triangular element in the mesh can be computed as

$$E = 0.5(C - I) \tag{16}$$

where I is the 2 x 2 identity matrix and C is the right Cauchy-Green deformation tensor, computed as $C=G^TgG$. Here, G and g are J^{-1} and j^{-1}, respectively, where J and j are the Jacobian matrices mapping the position of a point in global coordinates to the parametric representation adopted within a triangle, referred to the initial and current reference frame, respectively. Specifically,

$$g = \begin{pmatrix} (\Delta x^{21})^T \cdot \Delta x^{21} & (\Delta x^{21})^T \cdot \Delta x^{31} \\ (\Delta x^{21})^T \cdot \Delta x^{31} & (\Delta x^{31})^T \cdot \Delta x^{31} \end{pmatrix} \tag{17}$$

where Δx^{21} is the vector from vertex 1 to vertex 2 of the triangle in its present (deformed) configuration, and, similarly, Δx^{31} is the vector from vertex 1 to vertex 3. Matrix G is given by

$$G = \begin{pmatrix} \frac{1}{|\Delta X^{21}|} & \frac{-(\Delta x^{21})^T \cdot \Delta X^{31}}{|\Delta X^{21}||V_3|} \\ 0 & \frac{|\Delta X^{21}|}{|V_3|} \end{pmatrix} \tag{18}$$

where ΔX^{21} is the vector from vertex 1 to vertex 2 of the triangle in its original (undeformed) configuration, and, similarly, ΔX^{31} is the vector from vertex 1 to vertex 3. Vector V_3 is defined as the cross product of ΔX^{21} and ΔX^{31}.

The Green strain tensor computed using Eq. (16) describes strain relative to the local (triangle) coordinate system which, because of the unstructured nature of the triangle mesh, is arbitrarily oriented with respect to the global coordinate system. This tensor must be rotated to the principal axes of the tissue in order to apply the constitutive law in Eqns. (1-3) using

$$E' = R \begin{pmatrix} E_{11} \\ E_{22} \\ E_{12} \end{pmatrix} \tag{19}$$

where E_{ij} is the i,j^{th} component of the Green strain tensor and R is the strain transformation matrix given by

$$R = \begin{pmatrix} cos^2\theta & sin^2\theta & -2sin\theta cos\theta \\ sin^2\theta & cos^2\theta & 2sin\theta cos\theta \\ sin\theta cos\theta & -sin\theta cos\theta & cos^2\theta - sin^2\theta \end{pmatrix} \tag{20}$$

where θ is the angle between side ΔX^{21} of the triangle and the local fiber direction of the material measured in the original configuration of the mesh. Now the 2nd Piola-Kirchhoff stress tensor with respect to the principal axes of the tissue, S', is computed using the constitutive law given in Eqns. (1-3), and is then rotated back to the local reference frame using the inverse of transformation matrix R. Components of the local stress tensor, S, are then used to compute the forces on the nodes of the triangle due to internal forces as

$$f = -AHB^T \begin{pmatrix} S_{11} \\ S_{22} \\ S_{12} \end{pmatrix} \tag{22}$$

where A and H are the area and thickness of the triangle in its original configuration, and B is defined by

11

$$B=Qb \tag{23}$$

where Q is the stress transformation matrix, expressed in terms of the elements of G in Eq. (18)

as

$$Q = \begin{pmatrix} G_{11}^2 & 0 & 0 \\ G_{12}^2 & G_{22}^2 & G_{12}G_{22} \\ 2G_{11}G_{12} & 0 & G_{11}G_{22} \end{pmatrix} \tag{24}$$

and b is the 3x9 strain displacement matrix given as

$$b = \begin{pmatrix} -(\Delta x^{21})^T & (\Delta x^{21})^T & (0 \ \ 0 \ \ 0) \\ -(\Delta x^{31})^T & (0 \ \ 0 \ \ 0) & (\Delta x^{31})^T \\ -(\Delta x^{21}+\Delta x^{31})^T & (\Delta x^{31})^T & (\Delta x^{21})^T \end{pmatrix} \tag{25}$$

Thus, the nine elements of f from Eq. (22) are the three components of the force on vertex 1,

followed by those on vertices 2 and 3. The nodal force contributions from all triangles in the

mesh are summed to get the net internal forces on nodes throughout the mesh.

External Forces for Biaxial Loading. Biaxial loading was simulated by applying external

forces consisting of in-plane tensile loads distributed along edges of the square patch and aligned

perpendicular to the edge upon which they act with respect to the initial state of the mesh. Five

states of biaxial stress were simulated corresponding to ratios of peak Lagrangian stress in one

test axis to that in the other (perpendicular) axis of 20:60, 30:60, 60:60, 60:30, and 60:20 kPa

(Fig. 3). A biaxial loading protocol was simulated by applying forces to the edges of the patch to

maintain a constant ratio of Lagrangian stress between the two test axes. Simulations were

performed for fiber direction both coincident with one of the test axes and at 45° to it.

Since the system is dynamic, simulating a given loading curve involves running a dynamic

simulation at a series of incremental steps in applied stress and waiting until a steady-state is

reached at each step. For all simulated loading curves, we used increments of 0.025, 0.050, 0.1, 0.2, 0.4, 0.7, and 1.0 times the peak stress for that loading condition. Damping forces sufficient to critically damp all nodes in the mesh were added to each node in order to produce fast, stable simulations.

To determine the strain undergone by the deformed mesh, four virtual markers in the shape of a square, 1.5 mm on a side, were located in the center of the patch. Sides of the square were aligned with the fiber direction. For the undeformed state of the mesh, the location of each marker was computed in barycentric coordinates relative to the three vertices of the triangle containing it. During deformation, the positions of the markers were used to compute the components of Green strain. A given loading increment is determined to have converged when changes in both normal strains of the marker array become small (less than 2% of cumulative strain for that loading increment). The value of Lagrangian stress for that loading increment was converted to 2nd Piola-Kirchhoff stress, which, along with the value of Green strain from the marker array, was used to describe the constitutive behavior of the mesh as it is deformed.

External Forces for Pressure Loading. Pressure loading of the aortic valve mesh was simulated by applying a constant surface-normal pressure of 80 mmHg to all mesh triangles in the direction corresponding to radially inward (toward the axis of the cylinder) in the undeformed state of the mesh. All three semicircular leaflets are constrained by fixing all mesh vertices that lie on the semi-circumferences. Simulations are terminated when the incremental displacement of the middle of a leaflet free edge becomes small (below 10^{-5} mm).

Solution Method. The method used for discretizing and solving the system of equations is not critical to the aim of this study. We chose to discretize the equations using a second-order backward difference method [5] and solved using semi-implicit numerical integration with adaptive time-stepping [1]. A conjugate gradient method was used to solve the sparse linear system. Computation was implemented in the Matlab programming language (Mathworks, Natick, MA).

Results

A set of seven parameters describing the in-plane response of aortic valve leaflet tissue was generated by curve fits to the experimental data (Table 1). Deformation of a square patch using the FE model was simulated for five states of biaxial stress corresponding to ratios of Lagrangian stress in the *x*- to *y*-directions of 20:60, 30:60, 60:60, 60:30 and 60:20 kPa (Fig. 3). The final deformed states of the mesh are shown for the case where the material fiber direction coincides with the *x*-direction (Fig. 3, middle row) and where the material fiber direction is oriented at 45° to the *x*-direction in the undeformed configuration (Fig. 3, bottom row).

Plots of stress vs. strain were generated for the FE simulations (Fig. 4). For equibiaxial loading and normal strains (Fig. 4, middle row, columns 1 and 2), the mean error magnitude in strain for the FE simulations with respect to the actual constitutive law for the final loading increment is 0.004%. For non-equibiaxial loading states and normal strains (Fig. 4, rows 1, 2, 4 and 5, columns 1 and 2), the mean error magnitude in strain is 0.9%. For shear strains (Fig. 4, column 3), the mean error magnitude in strain is 3.1%. Note that for all of the stress vs. strain

plots for the FE simulations (Fig. 4), the standard deviations are so small that the gray region is very narrow and appears as a single curve.

Plots of stress vs. strain were generated for the M-S simulations (Fig. 5). For equibiaxial loading and normal strains (Fig. 5, middle row, columns 1 and 2), the mean error magnitude in strain for the M-S simulations with respect to the actual constitutive law for the final loading increment is 1.7%. For non-equibiaxial loading states and normal strains (Fig. 4, rows 1, 2, 4 and 5, columns 1 and 2), the mean error magnitude in strain is 7%. For shear strains (Fig. 4, column 3), the mean error magnitude in strain is 81%.

Pressure loading of a single aortic valve leaflet was simulated using the FE and M-S models and the final deformed state of the mesh was plotted for each (Fig. 6A and 6B). Two important metrics of leaflet deformation, free edge length and radial midline length, were computed for the deformed meshes and compared (Table 2). Differences in absolute position of the nodes of the two meshes were computed and mapped onto the nodes of the original (flattened) leaflet (Fig. 6C). Mean and maximum magnitudes of the difference in nodal position were 0.4 and 0.9 mm, respectively.

Pressure loading of a three leaflet aortic valve was simulated using the FE and M-S models, and the final deformed state of the mesh was plotted for each (Fig. 7A-D). A clinically important feature of the loaded valve is the extent of coaptation (i.e., overlap) between adjacent leaflets. We determine this for the two models shown by computing the distance between each mesh node and the nearest point on the surface of adjacent leaflets. Because repulsive contact forces are

used to handle self-collisions of leaflets, a gap of up to 1.5 mm can exist between leaflets that are in contact. The shape of the coaptation (contact) zone is estimated as the region enclosed by the contour line corresponding to an inter-leaflet distance of 1.5 mm (Fig. 7E). Maximum principal stress along with shear strain was plotted for the FE simulations of the full valve (Fig 8).

The computational cost of the two methods for computing internal forces was assessed in two ways. The first method involved counting the number of operations required to compute internal forces on the nodes of one triangle during one time step of the model. (Computation of all other components of the simulation was the same for the M-S and FE methods.) Operations were classified as multiplications (including divisions), additions (including subtractions), assignments, or other (e.g., square roots, inequalities, decisions, transcendental functions). The total number of floating point operations (FLOPs) was calculated by counting all operations as one FLOP except for square roots and transcendental functions, which were counted as 10 FLOPs each (Table 3). The second method involves measuring the actual time spent executing the portion of the program that performed these computations of internal forces. Execution time was then normalized by dividing by the execution time for the FE model (Table 3).

Discussion

The goal of this study was to develop an efficient M-S model that could simulate highly anisotropic membranes – about five times more distensible in one principal direction than in the other– on unstructured triangle meshes. Central to the development of this model was quantification of model speed and accuracy in order to assess its suitability for simulating heart valves as part of a surgical planning system. The M-S method examined here is faster but less

16

accurate than the simple FE model with which we compared it. However, the M-S model does reasonably well at approximating the deformation of a pressurized aortic valve with complex biomechanical properties, with simulated positions of leaflet nodes lying within 0.9 mm of nodal positions predicted by FE. Results of simulated biaxial loading illustrate the aspects of material behavior that the M-S model can and cannot accurately capture, while pressure loading simulations help assess model behavior as it is relevant for simulating a heart valve.

For the parameters listed in Table 1, the direct plots of the constitutive law for loading in the fiber direction (Fig. 4, left column, solid black circles) show that the stress-strain curves for the fiber direction move to the right as the applied stress increases in the fiber direction and decreases in the cross-fiber direction. The FE model incorporates the constitutive law directly and thus captures this behavior accurately (Fig. 4, left column, gray regions). Interestingly, dependence of the stress-strain curves on the overall state of stress is observed in the M-S model (Fig. 5, left column, gray regions), although curves are not as close to the actual constitutive equation as they are for the FE model, and variation due to the particular mesh discretization is greater. This dependence on the overall state of stress is probably due to the fact that the behavior in the two principal directions is entangled in the edge spring model as a result of the nearly continuous distribution of orientations of springs; forces in most of the edge springs have components in both principal directions. Plots of the constitutive law also show that the relationship between normal stress and strain is almost independent of shear strain (Fig. 4, middle column, solid black circles), as evidenced by the fact that all of the curves in the column are similar, despite a large positive shear strain in the top panel and large negative shear strain in

the bottom panel. This follows from the constitutive law parameters A_5 and A_6 being very close to zero.

The M-S model does a poor job of approximating shear stress (Fig. 5, third column). This is not surprising because our simple M-S model includes no shear springs and thus does not allow direct control of shear behavior. However, the state of loading of an actual heart valve leaflet under pressure load approximates equiaxial stress in regions away from constraints. This can be seen in the plot of leaflet shear strain produced by FE simulation (Fig. 8B), where the majority of the leaflet mesh exhibits shear strain of less than 0.1 (shear angle of approximately 6°), with the maximum value of 0.27 (shear angle of approximately 15°) occurring near the points of attachment of the leaflet free edge to the cylinder (aorta) wall.

Results of simulated pressure loading of the single leaflet model show that the overall shape of the deformed M-S mesh is very similar to that of the deformed FE mesh (Fig. 6, A and B). The most salient difference is the greater in-plane shear deformation in the M-S mesh near the constrained termini of the free edge (Fig. 6B). A consequence of this local region of exaggerated in-plane shear deformation is that the leaflet free edge is in a slightly lower position than in the FE mesh (Fig. 6A). This lower free edge combined with a slight bulging of the M-S mesh in the region just below the free edge results in the maximum discrepancy in nodal position of almost 1 mm (Fig. 6C). The computed length of the free edge of the deformed mesh is almost identical in the FE and M-S models, while the length of the radial midline is underestimated in the M-S model with respect to the FE model (Table 2). This reflects slightly decreased distension in the

M-S model in the cross-fiber direction and is also seen in the biaxial loading results (Fig. 5, right column, middle panel).

The FE simulations of the full aortic valve under pressure exhibit similar leaflet shape, and similar leaflet stress pattern and magnitude, to published studies [6, 14, 15]. M-S model simulations show very similar closed valve shape to the FE models. Again leaflet surfaces are somewhat smoother in the FE than the M-S model, and in-plane shear deformation appears to be larger in the M-S model near the points where the free edges are constrained (Fig. 7, panels A-D). The coaptation region is similar for the M-S and FE models, although its lower boundary is slightly "noisier" for the M-S model. The region predicted by the M-S model is somewhat narrow and is probably a manifestation of the position of the free edge due to the overestimation of in-plane shear.

Based both on counts of floating point operations and on compute times, the M-S model is about ten times faster than the FE model, a figure which agrees with published observations regarding speed comparison between M-S and FE methods[17, 32]. Our method of counting operations is approximate and neglects important computing details. For example, the number of clock cycles to compute a floating point addition is not typically the same as for division, and the cost of "other" (e.g., trigonometric) functions can vary with implementation. However, the relative proportion of the different categories of operations is similar between methods, so this relatively simple comparison should be valid. Likewise, the values for compute time depend on software and hardware factors, but a bias favoring one method is not apparent. It is important to note that the speed advantage to the M-S model is based only on the steps to compute nodal

forces due to deformation. If implicit methods are used to solve the equations of motion, Jacobian matrices must be computed for estimating future values of the nodal forces. The simplicity of the spring model formulations makes the computation of the Jacobians considerably simpler too, and it is likely that this would lead to further speed advantages for the M-S method. In fact, for the semi-implicit integration methods used for this study, the M-S model was typically 20 to 30 times faster than the FE model. However, we were unable to express the computational difference as a straightforward FLOP comparison due to the nature of the iterative conjugate gradient solution method and to the different time step histories produced by the M-S and FE simulation.

It is difficult to determine a maximum value of acceptable error for simulations in the context of a surgical planning system for heart valves. Valve repair surgery is not currently based on a quantitative approach that relates intraoperative valve dimensions to quantitative outcome measures of repair success. Errors due to the M-S modeling method of less than 1 mm seem small compared to overall valve dimensions, and are also a fraction of the coaptation height (overlap) characterizing normal valve closure. Still, many factors independent of the modeling method introduce uncertainty into patient-specific models, including mesh geometry and properties of the valve tissue (e.g., material fiber direction and constitutive behavior, both of which exhibit significant spatial variability within a given valve as well as between individuals). Any computational system used for surgical planning would have to undergo thorough validation to ensure accurate predictive value prior to clinical use.

While the constitutive law and valve geometry that were used in this study were for the aortic valve, the anisotropic M-S model could be used to simulate the other cardiac valves as well. In a previous study, we applied an isotropic version of M-S model to image-based meshes of the mitral valve[16]. While simulation results were validated against images of the closed valves, the fidelity of the M-S model with respect to in-plane shear was not assessed. The mitral valve, as well as the tricuspid, has many fibrous tethers (chordae tendineae) that attach to the leaflets. If chordae are modeled as linear segments attaching to the leaflets at single mesh nodes, high concentrated loads and significant local shear strain can result. In recent mitral valve modeling efforts, we have modeled chordae by distributing their leaflet insertion over several adjacent nodes rather than at a single node. In fact, this mimics the flaring of the actual chordae as they merge with the leaflets.

The M-S and FE models compared here are membrane formulations and, as such, provide no resistance to bending loads. However, this study is concerned with predicting the configuration of the closed valve at peak load when the leaflets are operating in the regime where in-plane stresses are relatively large - at least an order of magnitude greater than bending stresses [24, 33]. Another limitation concerns the use of bilinear models to approximate the constitutive law. These are valid only for the range of stresses used to compute parameters of the bilinear fit. For example, the exponential constitutive law presented here would predict continuing increases in membrane stiffness as stress increases above 50 kPa, but the bilinear functions maintain constant stiffness at these higher stresses. However, the constitutive law itself is not necessarily valid above that stress level, as it was produced by fits to experimental data over a similar range of stresses as used here. Another important limitation of the M-S model is the absence of control of

resistance to shear deformation. However, due to the way that heart valves are loaded and constrained, response to shear only appears to be important in limited regions close to point-constraints. Thus it is possible to avoid the computational burden of modeling shear behavior explicitly without paying a high price in terms of accuracy. In cases where the M-S model is used to predict deformation of valves following surgical modification, consequences of neglecting shear behavior could become more serious for cases where the repair results in valve anatomy or shear properties that differ significantly from that of a normal valve. Furthermore, we use a simplified, symmetrical model of the aortic valve, and model improvements accounting for asymmetries and complex aortic root behavior could change the pattern and /or magnitude of leaflet shear strain.

The anisotropic, nonlinear M-S model described here has been shown to simulate aortic valve leaflets under pressure load at considerable speed-ups with respect to an efficient FE membrane model and with only minor difference in the deformed state of the mesh. This difference in simulation time could enable a practical surgical planning system using present computing power. M-S systems lend themselves to being solved on parallel architectures because of the local nature of the forces between nodes [13], and several groups have developed methods for solving M-S systems on graphics processing units [12, 25, 31]. The computational advantages of M-S models combined with the speed-up of parallel computing may enable real-time surgical simulation of anisotropic heart valves in the near future.

Acknowledgements

References

1. Baraff, D. and A. Witkin. Large steps in cloth simulation. International Conference on Computer Graphics and Interactive Techniques :43-54, 1998.

2. Bianchi, G., B. Solenthaler, G. Szekely, and M. Harders. Simultaneous Topology and Stiffness Identification for Mass-Spring Models Based on FEM Reference Deformations. MICCAI :293-301, 2004.

3. Billiar, K. L. and M. S. Sacks. Biaxial mechanical properties of the natural and glutaraldehyde treated aortic valve cusp--Part I: Experimental results. J. Biomech. Eng. 122:23-30, 2000.

4. Bourguignon, D. and M. Cani. Controlling anisotropy in mass-spring systems. EGCAS :113-123, 2000.

5. Choi, K. and H. Ho. Stable but responsive cloth. ACM Transactions on Graphics 21:604-611, 2002.

6. Conti, C. A., A. Della Corte, E. Votta, L. Del Viscovo, C. Bancone, L. S. De Santo, and A. Redaelli. Biomechanical implications of the congenital bicuspid aortic valve: a finite element study of aortic root function from in vivo data. J. Thorac. Cardiovasc. Surg. 140:890-6, 896.e1-2, 2010.

7. Dal Pan, F., G. Donzella, C. Fucci, and M. Schreiber. Structural effects of an innovative surgical technique to repair heart valve defects. J. Biomech. 38:2460-2471, 2005.

8. Delingette, H. Triangular springs for modeling non-linear membranes. IEEE Transactions on Visualization and Computer Graphics 14:329-341, 2008.

9. Deussen, O., L. Kobbelt, and P. Tucke. Using simulated annealing to obtain good nodal approximations of deformable objects. Eurographics :30-43, 1995.

10. Field, D. A. Qualitative measures for initial meshes. Int. J. Num. Meth. Eng. 47:887-906, 2000.

11. Fung, Y. C. Biomechanics : mechanical properties of living tissues. New York: Springer-Verlag, 1993, 568 pp.

12. Georgii, J. and R. Westermann. Mass-spring systems on the GPU. Simulation Modelling Practice and Theory 13:693-702, 2005.

13. Gibson, S. F. F. and B. Mirtich. A survey of deformable modeling in computer graphics. TR-97-19:1-31, 1997.

14. Gnyaneshwar, R., R. K. Kumar, and K. R. Balakrishnan. Dynamic analysis of the aortic valve using a finite element model. Ann. Thorac. Surg. 73:1122-1129, 2002.

15. Grande, K. J., R. P. Cochran, P. G. Reinhall, and K. S. Kunzelman. Stress variations in the human aortic root and valve: the role of anatomic asymmetry. Ann. Biomed. Eng. 26:534-545, 1998.

16. Hammer, P. E., N. V. Vasilyev, D. P. Perrin, P. J. del Nido, and R. D. Howe. Fast image-based model of mitral valve closure for surgical planning. MICCAI Workshop on Computational Biomechanics for Medicine 3:15-26, 2008.

17. Keeve, E., S. Girod, R. Kikinis, and B. Girod. Deformable modeling of facial tissue for craniofacial surgery simulation. Comput. Aided Surg. 3:228-238, 1998.

18. Kim, H., K. B. Chandran, M. S. Sacks, and J. Lu. An experimentally derived stress resultant shell model for heart valve dynamic simulations. Ann. Biomed. Eng. 35:30-44, 2007.

19. Kunzelman, K. S., R. P. Cochran, C. Chuong, W. S. Ring, E. D. Verrier, and R. D. Eberhart. Finite element analysis of the mitral valve. J. Heart Valve Dis. 2:326-340, 1993.

20. Li, J., X. Y. Luo, and Z. B. Kuang. A nonlinear anisotropic model for porcine aortic heart valves. J. Biomech. 34:1279-1289, 2001.

21. Lim, K. H., J. H. Yeo, and C. M. Duran. Three-dimensional asymmetrical modeling of the mitral valve: a finite element study with dynamic boundaries. J. Heart Valve Dis. 14:386-392, 2005.

22. Lloyd, B. A., G. Szekely, and M. Harders. Identification of spring parameters for deformable object simulation. IEEE Transactions on Visualization and Computer Graphics 13:1081-1094, 2007.

23. May-Newman, K. and F. C. Yin. Biaxial mechanical behavior of excised porcine mitral valve leaflets. Am. J. Physiol. 269:H1319-27, 1995.

24. Merryman, W. D., H. Y. Huang, F. J. Schoen, and M. S. Sacks. The effects of cellular contraction on aortic valve leaflet flexural stiffness. J. Biomech. 39:88-96, 2006.

25. Mosegaard, J., P. Herborg, and T. S. Sorensen. A GPU accelerated spring mass system for surgical simulation. Stud. Health Technol. Inform. 111:342-348, 2005.

26. Prot, V., R. Haaverstad, and B. Skallerud. Finite element analysis of the mitral apparatus: annulus shape effect and chordal force distribution. Biomech. Model. Mechanobiol 8:43-55, 2009.

27. Ranga, A., R. Mongrain, Y. Biadilah, and R. Cartier. A compliant dynamic FEA model of the aortic valve. Proceedings of IFToMM, The 12th World Congress in Mechanism and Machine Science , 2007.

28. Sacks, M. S. A method for planar biaxial mechanical testing that includes in-plane shear. J. Biomech. Eng. 121:551-555, 1999.

29. Sacks, M. S. and A. P. Yoganathan. Heart valve function: a biomechanical perspective. Philos. Trans. R. Soc. Lond. B. Biol. Sci. 362:1369-1391, 2007.

30. Taylor, R. L., E. Oñate, and P. Ubach. "Finite Element Analysis of Membrane Structures." In: Textile composites and inflatable structures, edited by E. Oñate and B. Kröplin. , 2005, pp. 47-68.

31. Tejada, E. and T. Ertl. Large steps in GPU-based deformable bodies simulation. Simulation Modelling Practice and Theory 13:703-715, 2005.

32. Van Gelder, A. Approximate simulation of elastic membranes by triangulated spring meshes. Journal of Graphics Tools 3:21-42, 1998.

33. Vesely, I. and D. Boughner. Analysis of the bending behaviour of porcine xenograft leaflets and of natural aortic valve material: bending stiffness, neutral axis and shear measurements. J. Biomech. 22:655-671, 1989.

34. Votta, E., E. Caiani, F. Veronesi, M. Soncini, F. M. Montevecchi, and A. Redaelli. Mitral valve finite-element modelling from ultrasound data: a pilot study for a new approach to understand mitral function and clinical scenarios. Philos. Transact A. Math. Phys. Eng. Sci. 366:3411-3434, 2008.

35. Votta, E., A. Arnoldi, A. Invernizzi, R. Ponzini, F. Veronesi, G. Tamborini, M. Pepi, F. Alamanni, A. Redaelli, and E. G. Caiani. Mitral valve patient-specific finite element modeling from 3-D real time echocardiography: a potential new tool for surgical planning. MICCAI Workshop on Cardiovascular Interventional Imaging and Biophysical Modelling , 2009.

36. Watton, P. N., X. Y. Luo, X. Wang, G. M. Bernacca, P. Molloy, and D. J. Wheatley. Dynamic modelling of prosthetic chorded mitral valves using the immersed boundary method. J. Biomech. 40:613-626, 2007.

Table 1. Parameters of aortic valve leaflet constitutive law computed by fitting data from biaxial testing experiments.

Parameter	Value
c	9.7 Pa
A_1	49.558
A_2	5.2871
A_3	-3.124
A_4	16.031
A_5	-0.004
A_6	-0.02

Table 2. Comparison of dimensions of the deformed valve leaflet meshes predicted by the finite element (FE) and mass-spring (M-S) methods.
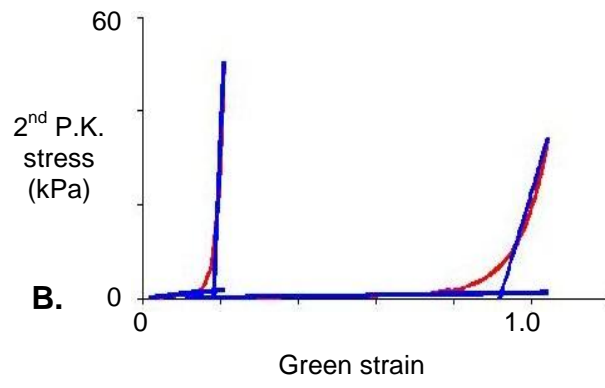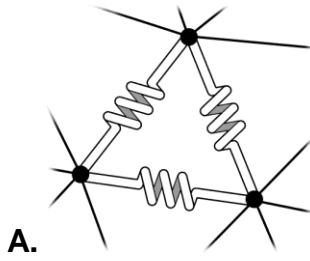
	Free edge length (mm) mean ± SD	Radial midline length (mm) mean ± SD
Undeformed Mesh	20.0	10.0
Mass-Spring	26.3 ± 0.2	15.2 ± 0.3
Finite Element	26.2 ± 0.02	15.6 ± 0.04

Table 3. Comparison of the computational cost of the finite element (FE) and mass-spring (M-S) models for computing internal forces. Operation counts and computation time are given per element per one time step of the dynamic simulation.

Method	x,÷	+,-	Assign	Other	FLOPs	Time re: FEM (%)
FEM	187	148	114	3	479	(100)
M-S	13	15	9	1	51	10

free edge
length

midline
length

Hammer et al. – Figure 1

A.

B.

2nd P.K. stress (kPa)

60

0

0   1.0

Green strain

Hammer et al. – Figure 2

A. P_y P_x

B. *fiber direction* 20:60 30:60 60:60 60:30 60:20
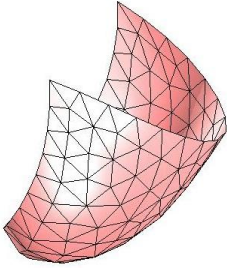
C. *fiber direction*
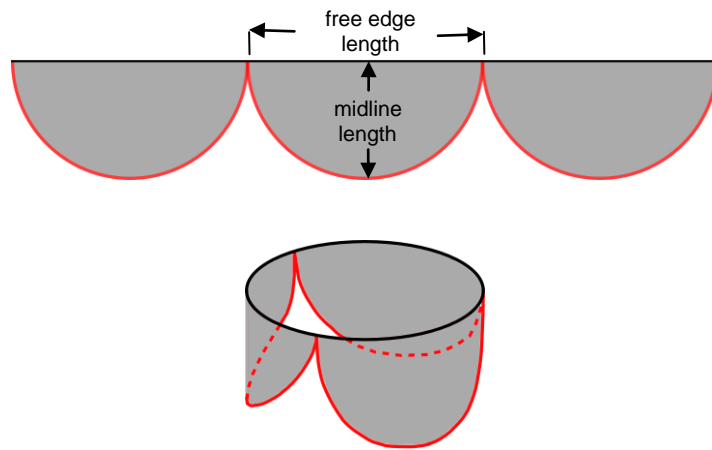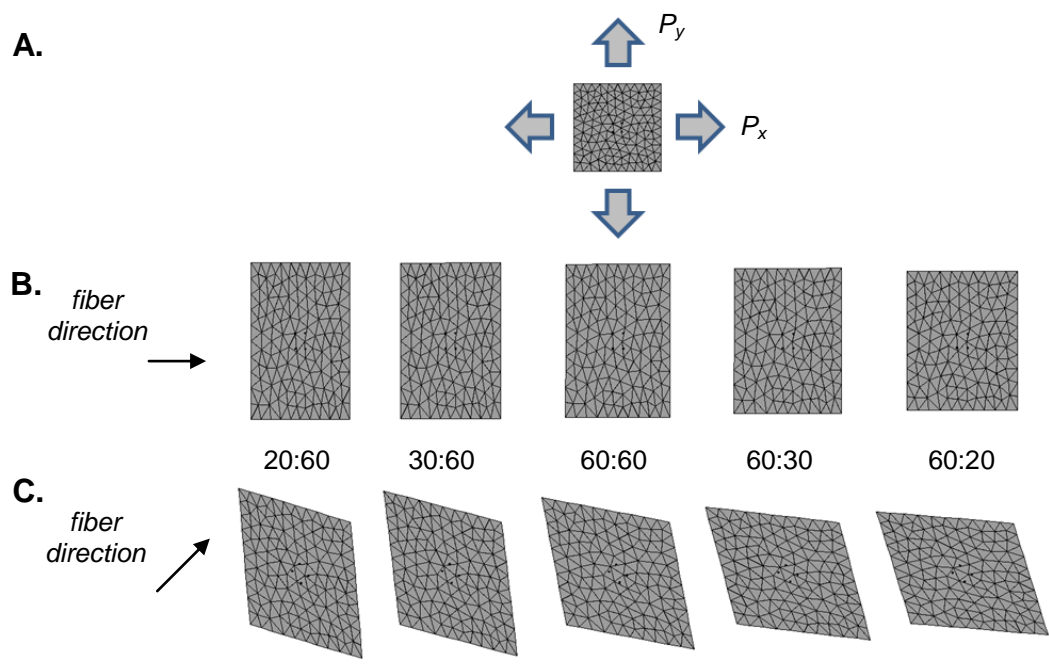
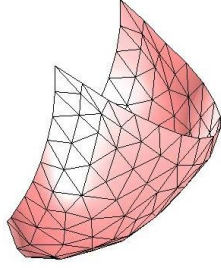Hammer et al. – Figure 3
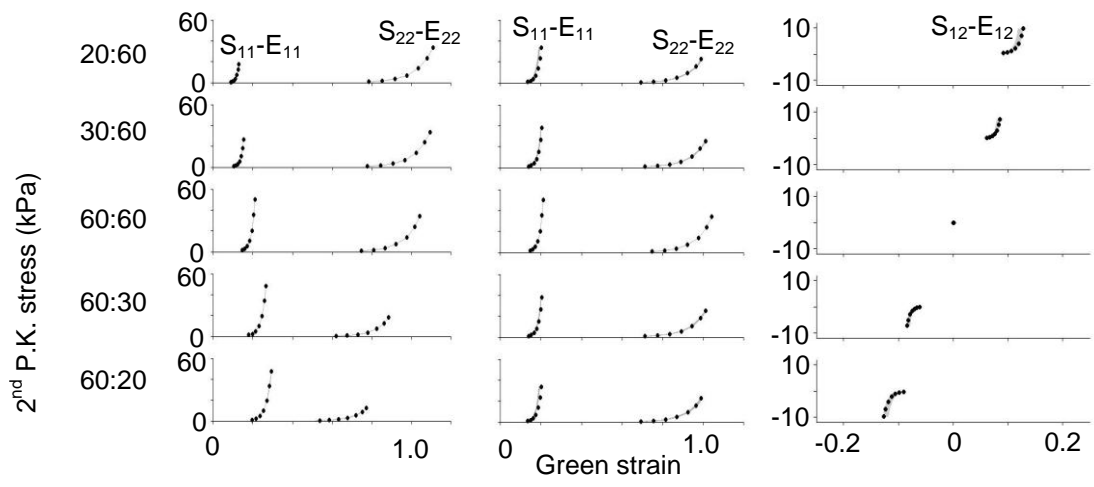
Hammer et al – Figure 4
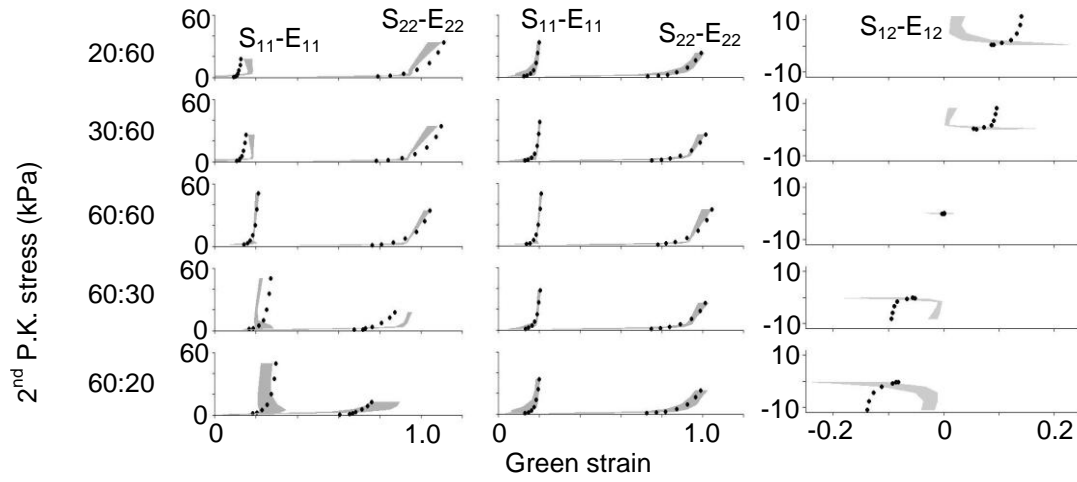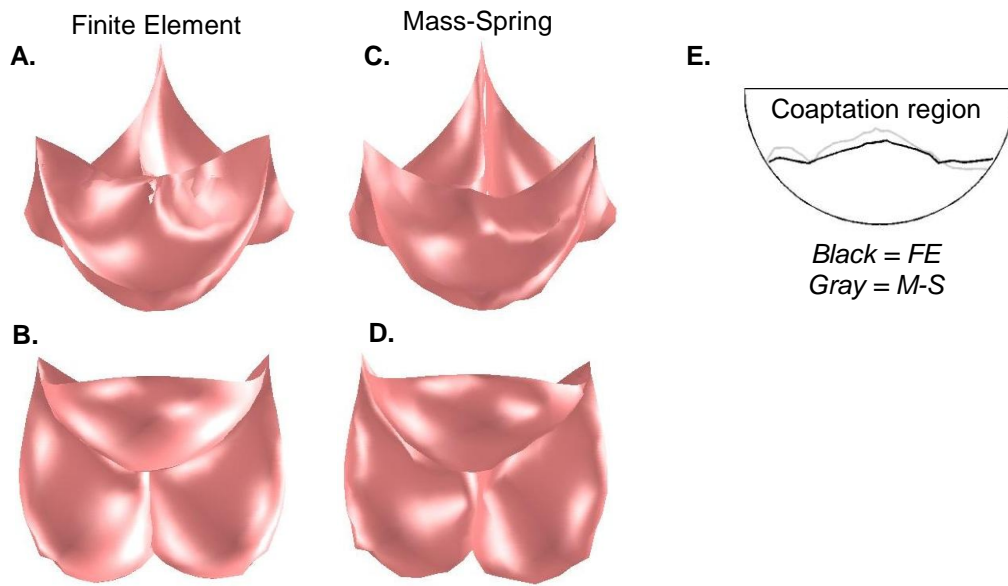
Hammer et al. – Figure 5

A. Finite Element

B. Mass-Spring

C. Distance magnitude (mm)

1.0

0

Hammer et al. – Figure 6

Finite Element

Mass-Spring

A.

C.

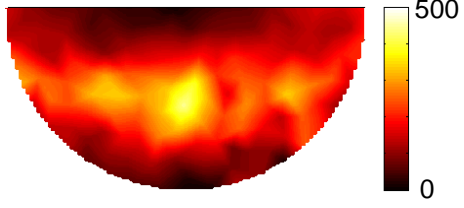**E.**

Coaptation region

Black = FE
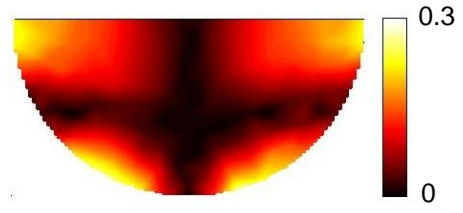*Gray = M-S*

B.

D.
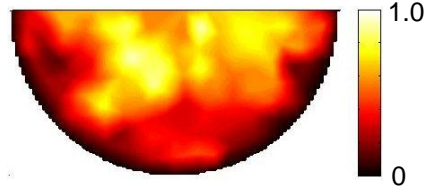
Hammer et al. – Figure 7

A. Max. Principal Stress (kPa)

B. Shear Strain

Hammer et al. – Figure 8

Figure 1. A single aortic valve leaflet is represented by a semicircle and a complete aortic valve as 3 semicircles arranged in a row (top sketch) then wrapped into a cylinder (bottom sketch) whose circumference is exactly three semicircle diameters. Each semicircular leaflet is constrained along its semicircumference by virtue of its attachment to the aortic root. This boundary is shown in red in both views. The top edge of each leaflet, whose length is equal to the semicircle diameter in the initial, unstressed state of the leaflet, is not attached to the aorta and is referred to as the leaflet free edge. This free edge length and the length of the leaflet midline are defined in the top sketch and are used to describe the degree of deformation of the leaflets. We assumed an unstressed leaflet diameter of 20 mm.

Figure 2. (A) Unstructured triangular meshes are treated as mass-spring systems by lumping the triangle mass at its vertices and treating all triangle edges as springs. (B) Spring constants are computed based on leaflet stiffness, which is approximated by a bilinear relationship with parameters determined by best fit to the phenomenological constitutive law.

Figure 3. Simulated deformation of a square patch of membrane under biaxial load. (A) Undeformed mesh showing directions of applied stresses, (B) Deformed mesh under the 5 states of biaxial stress $(P_x:P_y)$ = 20:60, 30:60, 60:60, 60:30, 60:20 kPa, where the material fiber direction coincides with the x-axis, (C) Deformed mesh under the same 5 states of stress but with the material fiber direction in the undeformed state oriented at 45° to the x-axis. All deformed meshes in this figure were produced using FE simulations.

Figure 4. Stress-strain curves for FE model. Second Piola-Kirchhoff stress in the fiber direction (S_{11}) and cross-fiber direction (S_{22}) is plotted as a function of Green strain for five biaxial loading curves. Loading states, determined by the ratio of peak Lagrangian stress in the x-direction to that in the y-direction, are, from top to bottom, 20:60, 30:60, 60:60, 60:30, and 60:20 kPa. The left column of plots shows normal stress vs. strain for the case where fiber direction coincides with the x-axis. The middle and right columns of plots show normal stress vs. strain and shear stress vs. strain for the case where the fiber direction is at 45° to the x-axis. The solid black circles represent the stress-stretch relationship calculated directly from the 7-parameter constitutive law. The gray curves represent the relationship computed from simulations and demarcate the mean strain ± one standard deviation at each of the stress increments across the 10 test meshes.

Figure 5. Stress-strain curves for the mass-spring (M-S) model. Second Piola-Kirchhoff stress in the fiber direction (S_{11}) and cross-fiber direction (S_{22}) is plotted as a function of Green strain for five biaxial loading curves. Loading states, determined by the ratio of peak Lagrangian stress in the x-direction to that in the y-direction, are, from top to bottom, 20:60, 30:60, 60:60, 60:30, and 60:20 kPa. The left column of plots shows normal stress vs. strain for the case where the fiber direction coincides with the x-axis. The middle and right columns show normal stress vs. strain and shear stress vs. strain for the case where the fiber direction is at 45° to the x-axis. The black solid circles represent the stress-strain relationship calculated directly from the 7-parameter constitutive law. The gray curves represent the relationship computed from simulations and demarcate the mean strain ± one standard deviation at each of the stress increments across the 10 test meshes.

Figure 6. The final deformed states of a simulated aortic valve leaflet subject to a static pressure load of 80 mmHg. The semicircular mesh is constrained along its semi-circumference. Images, from left to right, show the deformed leaflet simulated with the FE model, the deformed mesh simulated with the M-S model, and the discrepancy between the two deformed meshes expressed as the magnitude of the distance between corresponding nodes on the models and mapped onto the undeformed mesh.

Figure 7. The final deformed state of a simulated aortic valve (3 leaflets) subject to a static pressure load of 80 mmHg. Top oblique and bottom oblique views of the final deformed state of the mesh produced by the FE model are shown in panels A and B, respectively. The same views are shown for the M-S model in panels C and D. Panel E shows the coaptation region computed from the closed valve meshes for both models. The coaptation region is the portion of the semicircle bounded by the free edge on top and the irregular curve on the bottom.

Figure 8. (A) Maximum principal stress (kPa) in one leaflet of the pressure-loaded valve deformed by the FE model. (B) Magnitude of shear strain (Green strain) throughout the mesh of the pressure-loaded leaflet deformed using the FE model.